International Communications in Heat and Mass Transfer 171 (2026) 110072

Contents lists available at ScienceDirect

International Communications in Heat and Mass Transfer

journal homepage: www.elsevier.com/locate/ichmt

Investigation on PEMFC stack cathode gas maldistribution by an experiment-assisted improved flow network and computational fluid dynamics

Ren-Jie Yin [a,b], Fan Bai [a,b,*], Yu-tong Mu [c], Li Chen [a,b], Wen-Quan Tao [a,b,*]

[a] Key Laboratory of Thermo–Fluid Science and Engineering of Ministry of Education (XJTU), 710049, PR China
[b] School of Energy and Power Engineering, Xi'an Jiaotong University, Shaanxi, 710049, PR China
[c] School of Human Settlement and Civil Engineering, Xi'an Jiaotong University, 710049, PR China

ARTICLE INFO

Keywords:
Proton exchange membrane fuel cell stack
Cathode gas maldistribution
Computational fluid dynamic
Flow network method
Manifold design

ABSTRACT

This study aims to improve cathode gas distribution uniformity in a U-type 140-cell PEMFC stacks by developing an improved experimentally-assisted flow network method (IFNM) that combines computational efficiency with accuracy. The proposed improved flow network method (IFNM) replaces the traditional empirical correction for straight channels with a porous-medium pressure-drop model, providing a feasible framework for describing complex flow field resistance. An experimental-assisted explicit vapor-generation model is proposed and incorporated to account for the influence of electrochemical water production on gas distribution. The porous-medium parameters are experimentally identified from measured flowrate–pressure drop relationships and further validated under multiple operating conditions to ensure the reliability. Comparative results show that IFNM achieves less than 5 % deviation from three-dimensional CFD predictions of flow distribution while offering a two-order-of-magnitude reduction in computational time. Moreover, the IFNM introduces a geometry-based domain partition to distinguish bridge and reaction regions within the flow field, enabling a full-factor analysis of manifold cross-sectional and bridge geometric effects on distribution uniformity. The results demonstrate that manifold geometry is the dominant factor on cathode maldistribution, with the cross-sectional length and width showing strong positive correlations — simultaneous 20 % increases in both dimensions reduce the maldistribution indicator from 7.69 % to 3.64 %.

1. Introduction

As green energy is quickly boosted, proton exchange membrane fuel cell (PEMFC) is nowadays broadly adopted by the public transportation such as town buses and directed transport vehicles [1,2]. To meet industrial power requirements, multiple PEMFC unit cells are integrated into a stack configuration to deliver the necessary power output for target applications. The unit fuel cell's performance in the PEMFC stack differs from each other in the actual operation, which is because each cell receives different quantities of reactant gas due to the stack's maldistribution. The fuel cells receiving less reactant (air or hydrogen) shall generate inadequate power. The constant shortage of reactant of some unit cells not only reduces the total power supply, but may also eventually result in the reduction of the unit fuel cell server service life.

Researchers have developed different analysis model to study the gas maldistribution in the PEMFC stack. Park and Li [3] adopted the flow network method (FNM) and studied a non-isothermal PEMFC stack in 2006. Chen et al. [4] investigated a PEMFC stack by a simplified 2D model and regarded the gas channel as porous media in 2007. They claimed that the PEMFC stack's distribution will be improved with the increase of manifold cross-sectional area and of the unit cell's flow resistance. In 2015, Wang and Wang [5] proposed a discrete numerical model and summarized a group of dimensionless geometry parameters of the PEMFC stack to indicate the direction for improving gas distribution uniformity. In 2017, Amir et al. [6] applied the FNM for a 64-cell stack's cathode gas and temperature distribution analysis and revealed the influences of manifold section area, including the constant and gradient manifold cross-sectional area for both U and Z type configuration. The cross effect was studied in FNM by Qin et al. [7] in 2018. Based on a 200-cell stack, Huang et al. [8] took research on the gas maldistribution of cathode using porous medium model for the gas

* Corresponding authors.
E-mail addresses: fanbai@mail.xjtu.edu.cn (F. Bai), wqtao@xjtu.edu.cn (W.-Q. Tao).

https://doi.org/10.1016/j.icheatmasstransfer.2025.110072

Available online 17 November 2025

Nomenclature

A	bipolar plate active area (m^2)
C_2	Inertial resistance (m^{-1})
F	Faraday constant (96,485C.mol^{-1})
j_c	cathode current density (A.cm^{-2})
$K_g{}^{-1}$	Viscous resistance (m^{-2})
M	Molecular weight (g.mol^{-1})
q	Mass flow rate (kg.s^{-1})
N	Number of cells
n	Amount of substance (mol)
P	Statistic pressure (Pa)
R	Max-Min value
r	Flow resistance
RH	Relative humidity
ST_c	Stoichiometry
u	Velocity (m.s^{-1})
V_c	Volume of the gas channel (m^3)
Y	Mass fraction
ε	porosity
μ	Viscosity(Pa.s^{-1})
Re	Reynolds number
ρ	Density (kg.m^{-3})
φ	Volume fraction

Subscript

ave	Average value
b	Bridge
bin	Inlet bridge
bout	Outlet bridge
f	Friction loss
inf	Inlet face of the stack
in	Inlet manifold
j	Cell number
l	Local loss
m	Mass loss
max	Maximum
min	Minimum
outf	Outlet face of the stack
out	Outlet manifold
ra	Reaction area of flow field

channel in 2020. They discussed the distribution tendency in different types of stacks and compared the simulation result with experimental data. Further in 2021, Huang et al. [9] applied the conventional FNM on a stack's cathode with straight parallel flow field (SPFF) by both the FNM and CFD simulation for compare study. They use implicit modeling of the gas-liquid two-phase flow in SPFFs of a small-scale stack.

The geometric optimization of stack headers has become a new research direction for improving distribution uniformity. Su et al. [10] first highlighted the negative impact of header-induced vortex, proposing that strategic vortex positioning could enhance distribution. Chen et al. [11] applied neural networks, the Taguchi method, and Multivariate Adaptive Regression Splines (MARS) in a comparative framework to quantitatively assess the effects of header parameters on flow uniformity in a 30-cell stack, including the length ratio between connection pipes and header zones, header width, and pipe diameter.

Pan et al. [12] developed a 2D analytical model proposing rapid uniformity criteria for small scale stack with laminar-flow. Hossein et al. [13] established a novel cylindrical fuel cell design and a fractured membrane assembly. Both designs enhance performance by facilitating gas transport, as validated by simulation and experiment. Huang et al. [14] systematically analyzed a 160-cell U-type stack and evaluated the configurations of the headers. Their results revealed significant header geometry influences: stacks with tapered headers showed increased mass flow rates in inlet/outlet-proximate cells which will ameliorate the gas distribution. Bai et al. [15] applied Proper Orthogonal Decomposition (POD) to study eccentric header effects in a 140-cell stack's cooling channels, finding that maldistribution decreases with growing eccentricity magnitude while being less sensitive to eccentricity angle. Our previous work [16] on a 140-cell stack's anode hydrogen channels found symmetric headers outperformed asymmetric designs - contradicting Bai's conclusions and suggesting interference from other geometric parameters. Huang et al. [17] subsequently identified cooperative effects between manifold shape and inlet vortices, discovering specific length ratios for optimal uniformity. Xian et al. [18] also employed implicit modeling of the gas-liquid two-phase flow in the channels of a small-scale stack, utilizing a two-phase multiplier approach. Yu et al. [19] optimizes the manifold of a high-power fuel cell stack using a DBO algorithm, identifying a "ZZZ" configuration that significantly improves performance consistency. This optimization enables a 63.6 % increase in stack rated power, demonstrating a viable path for enhancing high-power fuel cell systems. Nima et al. [20] introduces novel asymmetric flow channels for PEMFCs, optimized through a combined analytical, numerical and AI-driven approach. The optimal design significantly enhances performance, achieving a 5.6 % increase in current density. Ahmad et al. [21] found that oxygen distribution is most even in the UZ configuration, superior to U and Z types. While independent of pressure and flow rate in the U configuration, manifold width changes affect all configurations differently.

Research on PEMFC stack flow maldistribution primarily employs three approaches: computational fluid dynamics (CFD), the flow network method (FNM), and 2D analytical modeling. Currently, 3D CFD simulations are widely used to study complex flow fields (e.g., serpentine or interdigitated designs) in commercial PEMFC stacks. These flow fields generate higher pressure drops, improving water management and gas distribution uniformity. However, CFD requires substantial computational resources and time, making it impractical for rapid design iterations.

In contrast, FNM offers fast calculations but is limited to simple flow fields like straight parallel flow fields (SPFFs). Since SPFFs have low pressure drops, they suffer from severe flow maldistribution (up to 60–70 % deviation in 200-cell stacks). Traditional FNM relies on empirical pressure drop formulas, which are unavailable for complex flow fields, restricting its applicability. Regarding the more complex flow fields, the related FNM studies such as [18] primarily employs a fitting-based approach, using the $AU^2 + BU$ general format to calibrate channel pressure drop, and lacks validation with large-scale stack experimental data as well as reliability test for parameter robustness. For the water produced in fuel cells, former studies [8] [18] assumed inlet gas at 100 % relative humidity, which leads to the immediate formation of liquid water. The liquid water influence implicitly accounts for the resulting pressure drop via a two-phase multiplier in single-cell channels, while neglecting the impact of generated water in any form in the outlet manifold on flow distribution. These assumptions have significant limitations in real stack operation, where the inlet gas is often undersaturated, and a substantial portion of the product water exists in vapor form. This generated water vapor, as part of the gaseous phase, must also be considered for its influence on distribution characteristics.

To bridge the methodological gap between conventional CFD and FNM approaches, this study develops an improved flow network method (IFNM) that simultaneously overcomes their respective limitations,

enabling fast yet high-fidelity flow distribution analysis in PEMFC stacks.

In the proposed framework, the simplified regions of the stack are modeled using a standard porous-medium pressure-drop formulation, replacing the empirical correlations typically adopted for straight parallel flow fields (SPFFs). Meanwhile, explicit vapor generation terms are incorporated to represent electrochemical water production based directly on experimentally derived data, rather than empirical correction multiplier. Furthermore, the porous-medium parameters are quantitatively identified from experimental pressure drop, and the reliability of these fitted parameters is validated with additional experimental datasets. The improved IFNM is applied to a commercial 140-cell U-type PEMFC stack cathode (Fig. 1), demonstrating distribution uniformity prediction comparable to full CFD simulations under identical assumptions, while reducing computational cost by orders of magnitude.

Importantly, the IFNM explicitly distinguishes manifold, bridge, and flow-field subdomains, thereby enabling detailed assessment of manifold and bridge geometric influences on gas distribution, which is generally inaccessible to traditional FNMs.

The remainder of this paper is structured as follows. Section 2 presents the mathematical formulations of IFNM and CFD framework. Section 3 describes the numerical methodology employed in the CFD simulations and the experimental setup used for the PEMFC stack test. Section 4 provides a comparative discussion of the results from the IFNM and CFD approaches. The paper concludes with key findings and conclusions in Section 5.

2. Mathematical model of the IFNM and CFD

2.1. Basic assumptions adopted

This study adopts following assumptions in both IFNM and CFD:

1) The influence of liquid water is neglected. This is a widely adopted assumption not only in the study of flow maldistribution, but also in the study of PEMFC performance of single-cell [22–28] based on the consideration that the high gas velocity could move the liquid water drops soon leave the channel.

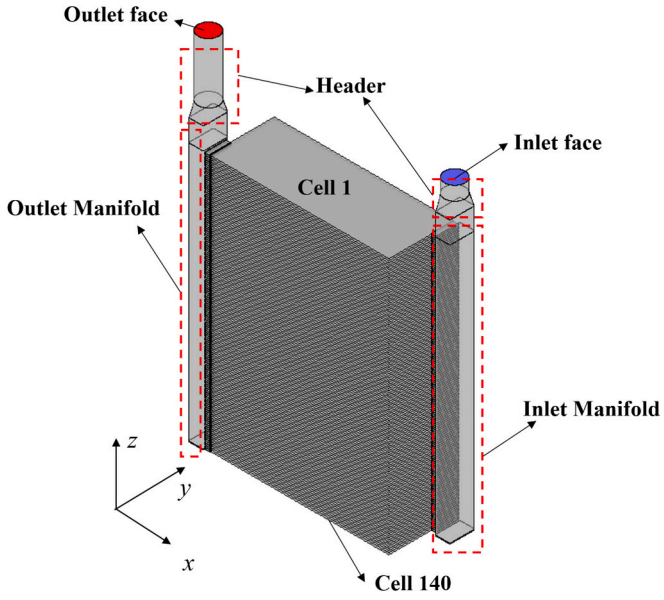

Fig. 1. The geometry of the 140-cell stack's cathode.

2) The temperature across the entire domain is assumed constant; consequently, the thermophysical properties of the gas mixture remain constant.
3) The oxygen is assumed to be uniformly consumed and the water vapor is assumed to be uniformly generated along the channel direction in the simplified porous medium. It is to be noted that uniform assumption of oxygen seems unreasonable. However, to the authors' knowledge only for single-cell study the distributions of different components may be studied in detail. For a stack with hundreds of single-cell to resolute the component distribution in each cell is impossible because of computer resource limitation and locally uniform distribution is a feasible assumption. [14–17]
4) The process is of steady-state. Although there are also several unsteady operation processes in the life cycle of PEMFCs, the maldistribution studies in literature are based on steady state to prevent the cells from long-time starvation state.
5) The gravity influence, internal thermal conduction, membrane hydration processes, and cavity-to-cavity thermo-mechanical coupling are not considered [14–17].

2.2. Model of the Improved Flow Network Method (IFNM)

The oxygen mass flow rate at cathode's inlet is shown by Eq. (1). According to the oxygen volume fraction in air φ_{O_2} and air's molar weight M_{air}, the inlet air mass flow rate is introduced as Eq. (2).

$$q_{O_2,inf} = 1000 \cdot N \cdot \frac{j_c \cdot A_{bp} \cdot ST_c}{4F} \cdot M_{O_2} \tag{1}$$

$$q_{air,inf} = \frac{q_{O_2,inf}}{M_{O_2}} \cdot \varphi_{O_2} \cdot M_{air} \tag{2}$$

The vapor partial pressure at the inlet is determined based on the saturated vapor pressure at the inlet temperature and the relative humidity of the inlet gas. The vapor mass flow rate at inlet is further derived from vapor partial pressure shown in Eq. (3). The total mass flow rate at the inlet is shown as Eq. (4).

$$q_{vap,inf} = \frac{n_{air,inf} RH_{inf} P_{sat}(T_{inf})}{P_{inf} - RH_{inf} P_{sat}(T_{inf})} \cdot M_{H_2O} \tag{3}$$

$$q_{c,inf} = q_{air,inf} + q_{vap,inf} \tag{4}$$

The mean values of thermophysical properties, including density and viscosity, at both the inlet and outlet are adopted as follows. The density is determined based on the local mass fraction of air and vapor at the inlet and outlet, respectively. For the average dynamic viscosity, a power-law formulation is applied to interpolate between the values computed at the corresponding inlet and outlet temperatures.

$$\rho_{inf} = \frac{M_{air}(P_{inf} + P_0 - RH_{in} \cdot P_{sat}(T_{inf})) + M_{vap} \cdot RH_{in} \cdot P_{sat}(T_{inf})}{R_g T_{inf}} \tag{5}$$

$$\rho_{outf} = \frac{M_{air}(P_{outf} + P_0 - RH_{outf} \cdot P_{sat}(T_{outf})) + M_{vap} \cdot RH_{out} \cdot P_{sat}(T_{outf})}{R_g T_{outf}} \tag{6}$$

$$\rho_{mix} = \frac{\rho_{inf} + \rho_{outf}}{2} \tag{7}$$

$$\mu_{mix} = 4.842 \times 10^{-7} \frac{T_{inf}^{0.6392} + T_{outf}^{0.6392}}{2} \tag{8}$$

For the convenience of the iteration IFNM, the unit cells are numbered from 1 to 140 as shown in Fig. 2, and this numbering method is only used in this section for analytical model. In the subsequent result analysis for the IFNM result of gas maldistribution, cells are still numbered according to Fig. 1 for the sake of comparability of both CFD and IFNM methods.

According to the mass conservation law, for the U-type stack, the

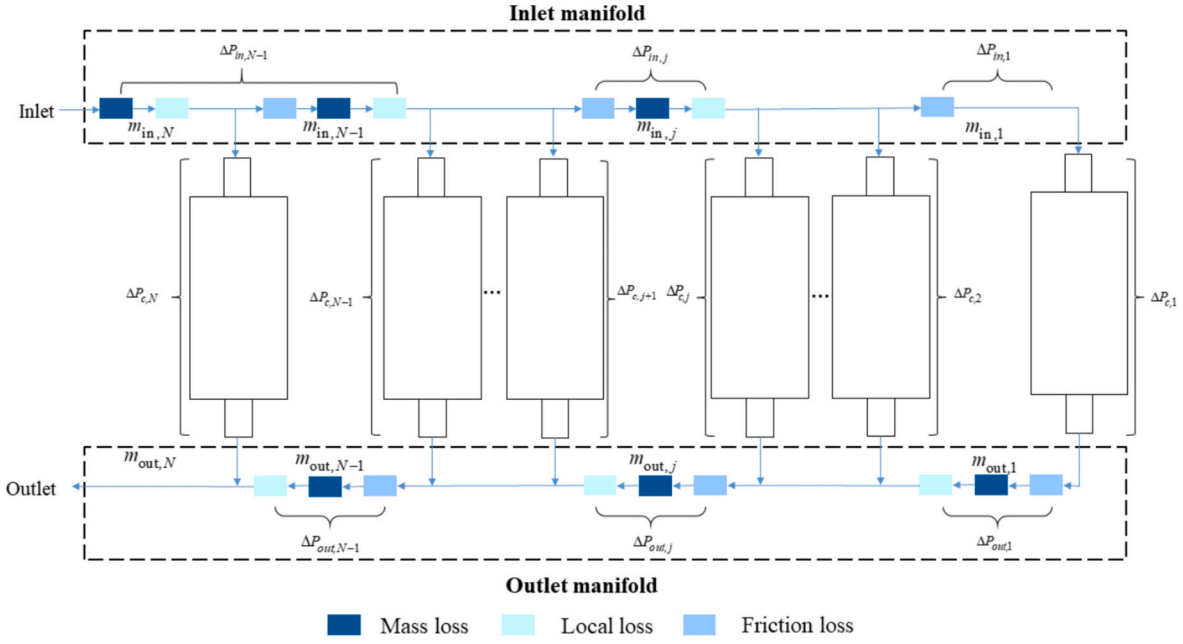

Fig. 2. Schematic diagram of pressure drop model for U-type stack cathode of IFNM.

mass flow rate through each segment between adjacent porous media within the inlet and outlet manifolds is given by Eqs. (9,10), respectively. In the equations $q_{\mathrm{bin},j}$ and $q_{\mathrm{bout},j}$ are the mass flow rate at the unit cell's inlet and outlet bridge, respectively, which will be introduced later.

$$q_{\mathrm{in},j} = q_{\mathrm{in},j-1} + q_{\mathrm{bin},j} \tag{9}$$

$$q_{\mathrm{out},j} = q_{\mathrm{out},j-1} + q_{\mathrm{bout},j} \tag{10}$$

The mass flow rate at the inlet manifold entrance is equal to the cathode total inlet mass flow rate, as defined by Eq. (11). Similarly, the gas mass flow rate at the outlet manifold corresponds to the value at the cathode outlet, given in Eq. (12) It includes the oxygen consumption $q_{\mathrm{c,O_2}}$ and explicit vapor generation $q_{\mathrm{c,vap}}$ in the stack's cathode. These two terms will be introduced in the next part of CFD model.

$$q_{\mathrm{in},N} = q_{\mathrm{c,inf}} \tag{11}$$

$$q_{\mathrm{out},N} = q_{\mathrm{c,inf}} - N\left(q_{\mathrm{c,O_2}} + q_{\mathrm{c,vap}}\right) \tag{12}$$

The pressure drops in both the inlet and outlet manifold are also displayed in Fig. 2. As Eqs. (13, 14) show, the pressure change $\Delta P_{\mathrm{in,j}}$, $\Delta P_{\mathrm{out,j}}$ in each segment of the manifold consists of the pressure change due to mass transfer $\Delta P_{\mathrm{m},j}$ and the pressure loss including the local loss $\Delta P_{\mathrm{l},j}$ and the friction loss $\Delta P_{\mathrm{f},j}$.

$$\Delta P_{\mathrm{in},j} = \Delta P_{\mathrm{in,m,j}} + \Delta P_{\mathrm{in,f,j}} + \Delta P_{\mathrm{in,l,j}} \tag{13}$$

$$\Delta P_{\mathrm{out,j}} = \Delta P_{\mathrm{out,m,j}} + \Delta P_{\mathrm{out,f,j}} + \Delta P_{\mathrm{out,l,j}} \tag{14}$$

where $\Delta P_{\mathrm{m},j}$and $\Delta P_{\mathrm{f},j}$ are expressed as Eqs. (15, 16), respectively. The value of mass loss in the inlet manifold $\Delta P_{\mathrm{in,m,j}}$ is negative while the value of mass loss in the outlet manifold $\Delta P_{\mathrm{out,m,j}}$ is positive.

$$\Delta P_{\mathrm{m},j} = \Delta\left(\frac{\rho_{\mathrm{mix}} u_j^2}{2}\right) \tag{15}$$

$$\Delta P_{\mathrm{f},j} = \lambda \rho_{\mathrm{mix}} \frac{\Delta L}{D} \frac{u_j^2}{2} \tag{16}$$

Local pressure losses are expressed as Eq. (17, 18) for the inlet and outlet manifold respectively, in which the local loss coefficients $K_{\mathrm{in,l},j}$, $K_{\mathrm{out,l},j}$ are based on Bassett et al.'s study [29].

$$\Delta P_{\mathrm{in,l},j} = \rho_{\mathrm{mix}} K_{\mathrm{in,l},\ j} \frac{u_{\mathrm{in},j}^2}{2} \tag{17}$$

$$\Delta P_{\mathrm{out,l},j} = \rho_{\mathrm{mix}} K_{\mathrm{out,l},j} \frac{u_{\mathrm{out},j}^2}{2} \tag{18}$$

The total pressure change of each inlet manifold segment is derived from Eq. (13) and Eqs. (15–17).

$$\Delta P_{\mathrm{in},j} = \rho_{\mathrm{mix}}\left(r_{\mathrm{in},1} q_{\mathrm{in},j}^2 + r_{\mathrm{in},2} q_{\mathrm{in},j}^{1.75} + r_{\mathrm{in},3} q_{\mathrm{in},j-1} q_{\mathrm{in},j} + r_{\mathrm{in},4} q_{\mathrm{in},j-1}^2\right) \tag{19}$$

The same derivation procedure is carried out for each outlet manifold segment from Eq. (14), Eqs. (15–16) and Eq. (18) into Eq. (20).

$$\Delta P_{\mathrm{out},j} = \rho_{\mathrm{mix}}\left[r_{\mathrm{out},1}\left(q_{\mathrm{out},j-1}^2 - q_{\mathrm{out},j}^2\right) + r_{\mathrm{out},2} q_{\mathrm{out},j}^{1.75}\right] \tag{20}$$

The related flow resistance parameters in Eqs. (19–20) including are quoted from Huang's work [9].

The porous medium is divided into three continuous parts as Fig. 3, which represents the unit cell's inlet bridge, flow filed, and outlet bridge, respectively. The geometric sizes of the three parts are the same as the CFD model displayed in the subsequent part.

The porous medium is departed to distinguish and accurately define the mass flow rate change in different parts. The inlet bridge's mass flow rate $q_{\mathrm{bin},j}$ is treated as the same quantity of gas entering from inlet manifold with neither oxygen consumed nor vapor generated. The outlet bridge's mass flow rate $q_{\mathrm{bout},j}$ is treated as the one after flowing out of the reaction area as shown by Eq. (21) in which the oxygen has been consumed and vapor has been generated. The reaction area's mass flow rate $q_{\mathrm{ra},j}$ is taken as the average value of them two as shown by Eq. (22).

$$q_{\mathrm{bout},j} = q_{\mathrm{bin},j} - q_{\mathrm{c,O_2},j} + q_{\mathrm{c,vap},j} \tag{21}$$

$$q_{\mathrm{ra},j} = \frac{q_{\mathrm{bin},j} + q_{\mathrm{bout},j}}{2} \tag{22}$$

Fig. 3 separately illustrates the pressure variations across different components in the cathode flow field, along with their underlying causes. The total pressure change is shown in Eq. (23), which consists of the following four parts: (1) the friction loss of gas flowing through the

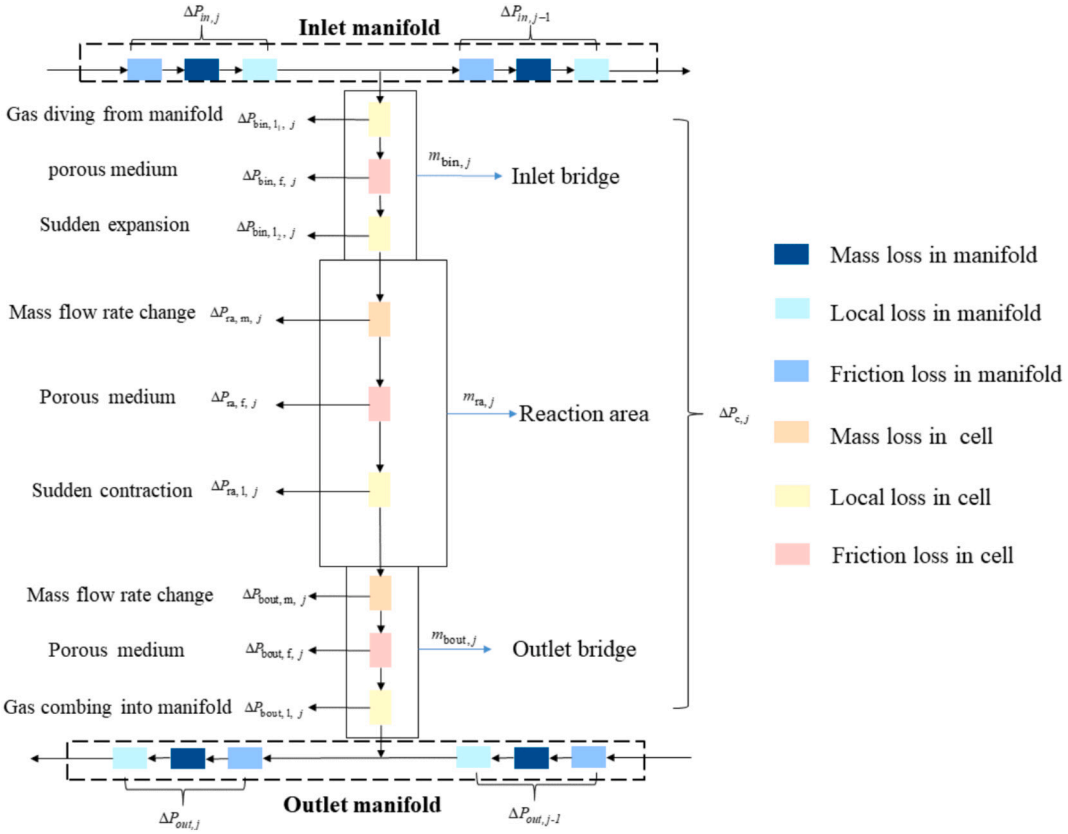

Fig. 3. The simplified porous medium model of the gas channel.

three parts of porous medium $\Delta P_{\mathrm{bin,f},j}$, $\Delta P_{\mathrm{ra,f},j}$ and $\Delta P_{\mathrm{bout,f},j}$, (2) the local losses $\Delta P_{\mathrm{bin,l_1},j}$ and $\Delta P_{\mathrm{bout,l},j}$ that are generated when the gas divides and combines between the manifold and the porous medium zone of the bridge, (3) the local loss $\Delta P_{\mathrm{bin,l_2},j}$ and $\Delta P_{\mathrm{ra,l},j}$ that are generated when the gas comes to the sudden expansion and sudden contraction area, and (4) the mass loss $\Delta P_{\mathrm{ra,m},j}$ and $\Delta P_{\mathrm{bout,m},j}$ arised from the variation of mass flow rate.

$$\Delta P_{\mathrm{c},j} = \Delta P_{\mathrm{bin,l_1},j} + \Delta P_{\mathrm{bin,f,j}} + \Delta P_{\mathrm{bin,l_2,j}} + \Delta P_{\mathrm{ra,m,j}} + \Delta P_{\mathrm{ra,f,j}} + \Delta P_{\mathrm{c,l_1},j} + \Delta P_{\mathrm{ra,l,j}} + \Delta P_{\mathrm{bout,m,j}} + \Delta P_{\mathrm{bout,f,j}} + \Delta P_{\mathrm{bout,l},j} \tag{23}$$

The pressure drop created when flowing through the porous medium are displayed in Eqs. (24–26), in which $\frac{1}{K_g}$is the viscous resistance and C_2 represents the inertial resistance.

$$\Delta P_{\mathrm{bin,f},j} = \frac{1}{K_g}\mu_{\mathrm{mix}}\frac{q_{\mathrm{bin},j}}{\rho_{\mathrm{mix}}A_{\mathrm{b}}}L_{\mathrm{bin}} + \frac{C_2}{2}\rho_{\mathrm{mix}}\left(\frac{q_{\mathrm{bin},j}}{\rho_{\mathrm{mix}}A_{\mathrm{b}}}\right)^2 L_{\mathrm{bin}} \tag{24}$$

$$\Delta P_{\mathrm{ra,f},j} = \frac{1}{K_g}\mu_{\mathrm{mix}}\frac{q_{\mathrm{ra},j}}{\rho_{\mathrm{mix}}A_{\mathrm{ra}}}L_{\mathrm{ra}} + \frac{C_2}{2}\rho_{\mathrm{mix}}\left(\frac{q_{\mathrm{ra},j}}{\rho_{\mathrm{mix}}A_{\mathrm{ra}}}\right)^2 L_{\mathrm{ra}} \tag{25}$$

$$\Delta P_{\mathrm{bout,f},j} = \frac{1}{K_g}\mu_{\mathrm{mix}}\frac{q_{\mathrm{bout},j}}{\rho_{\mathrm{mix}}A_{\mathrm{b}}}L_{\mathrm{bout}} + \frac{C_2}{2}\rho_{\mathrm{mix}}\left(\frac{q_{\mathrm{bout},j}}{\rho_{\mathrm{mix}}A_{\mathrm{b}}}\right)^2 L_{\mathrm{bout}} \tag{26}$$

The local pressure losses can be expressed in Eqs. (27–30):

$$\Delta P_{\mathrm{bin,l_1},j} = \rho K_{\mathrm{bin,l_1},j}\frac{u_{\mathrm{bin},j}^2}{2} \tag{27}$$

$$\Delta P_{\mathrm{bin,l_2},j} = \rho K_{\mathrm{bin,l_2},j}\frac{u_{\mathrm{bin},j}^2}{2} \tag{28}$$

$$\Delta P_{\mathrm{ra,l},j} = \rho K_{\mathrm{ra,l},j}\frac{u_{\mathrm{ra},j}^2}{2} \tag{29}$$

$$\Delta P_{\mathrm{bout,l},j} = \rho K_{\mathrm{bout,l},j}\frac{u_{\mathrm{bout},j}^2}{2} \tag{30}$$

The local loss coefficient $K_{\mathrm{bin,l_1},j}$ and $K_{\mathrm{bout,l},j}$ in Eqs. (27, 28) can be determined by empirical formulas for laminar flow [9,30]. The local loss coefficient $K_{\mathrm{bin,\ l_2},j}$ and $K_{\mathrm{ra,l},j}$ in Eqs. (28, 29) can be determined by empirical formulas from work [31]. They are shown in Eqs. (31–34).

$$K_{\mathrm{bin,l},j} = \frac{276}{\mathrm{Re}_{\mathrm{bin},j}}\left(\frac{u_{\mathrm{bin},j}}{u_{\mathrm{in},j}}\right)^2 \tag{31}$$

$$K_{\mathrm{bin,l_2},j} = \left(1 - \frac{A_{\mathrm{b}}}{A_{\mathrm{c}}}\right)^2 \tag{32}$$

$$K_{\mathrm{ra,l},j} = 0.5\left(1 - \frac{A_{\mathrm{b}}}{A_{\mathrm{c}}}\right) \tag{33}$$

$$K_{\mathrm{bout,l},j} = \frac{72}{\mathrm{Re}_{\mathrm{bout},j}}\left(\frac{u_{\mathrm{bout},j}}{u_{\mathrm{out},j}}\right)^2 \tag{34}$$

According to the Hardy cross method [32] which aims to apply the iteration process to obtain the gas distribution in the flow network, each two neighboring cells and the segment of inlet and outlet manifold that connects them could form a loop for whom the total static pressure change should sum up to be zero according to the momentum conservation equation. For the U type stack, this relationship is expressed in Eq. (35).

$$\mathrm{loop}_j = \Delta P_{\mathrm{in},j} + \Delta P_{\mathrm{c},j} + \Delta P_{\mathrm{out},j} - \Delta P_{\mathrm{c},j-1} = 0, (j = 2, 3, \ldots, N) \tag{35}$$

At the start of the iterative process, an initial value for the mass flow

rate in each unit cell is assigned based on the average total inlet mass flow rate divided by the number of cells. Subsequently, these values are updated iteratively. According to the Hardy cross method, $loop_j$'s absolute value in each loop should be lower than a predetermined threshold of 10^{-10} Pa. During each iteration, $loop_j$ is continuously monitored to accordingly adjust the mass flow rate for the next turn. If $loop_j$ exceeds the threshold of 10^{-10} Pa, it indicates the mass flow rate of the cell of this particular loop from last iteration is higher than the actual value. To address, the mass flow rate in next iteration should be adjusted downward, taking the average of the current value and zero. Conversely, when $loop_j$ falls below the threshold of -10^{-10}, the mass flow rate in next iteration should be adjusted upward, taking the average of the current value and total mass flow rate. When the specified residual of all the loops is satisfied, the whole iteration process is regarded as fully converged.

2.3. Governing equations and boundary conditions of CFD method

For the 3D CFD model, the conservation equations are presented in Eqs. (36–38), respectively. The standard k-ε equations are applied in all the computational domain except the porous medium zone in the 140-cell cathode.

$$\nabla\cdot\left(\varepsilon\rho_g\vec{u}_g\right)=S_m \tag{36}$$

$$\nabla\cdot\left(\frac{\rho_g\vec{u}_g\vec{u}_g}{\varepsilon^2}\right)=-\nabla p_g+\mu_g\nabla\cdot\left(\nabla\left(\frac{\vec{u}_g}{\varepsilon}\right)+\left(\frac{\vec{u}_g^{\,T}}{\varepsilon}\right)\right)-\frac{2}{3}\mu_g\nabla\left(\nabla\cdot\left(\frac{\vec{u}_g}{\varepsilon}\right)\right)+\mathbf{S}_u \tag{37}$$

$$\nabla\cdot\left(\rho_g\vec{u}_gY_i\right)=\nabla\cdot\left(\rho_gD_i^{eff}\nabla Y_i\right)+S_i \tag{38}$$

The source term of mass conservation equation in Eq. (36) is expressed as Eq. (39).

$$S_m=S_{O_2}+S_{vap} \tag{39}$$

The oxygen and vapor terms on the right of Eq. (35) are their own species source terms in their respective species conservation equations. The oxygen source term is expressed as Eq. (40) according to the PEMFC model.

$$S_{O_2}=-\frac{j_c}{4F}M_{O_2}\frac{A_{ra}}{V_c} \tag{40}$$

Thus, it is able to get the oxygen consumed by each unit cell and by the whole stack as Eqs. (41, 42). Further, the mass flow rate of oxygen at the cathode's outlet can be derived as Eq. (43).

$$q_{c,O_2}=10^6S_{O_2}V_c \tag{41}$$

$$q_{O_2,con}=N\cdot q_{c,O_2} \tag{42}$$

$$q_{O_2,outf}=q_{O_2,inf}-q_{O_2,con} \tag{43}$$

The mass flow rate of air and its amount of substance at the stack's outlet is written as Eqs. (44, 45).

$$q_{air,outf}=q_{O_2,outf}+q_{air,inf}-q_{O_2,inf} \tag{44}$$

$$n_{air,outf}=\frac{q_{O_2,outf}}{M_{O_2}}+\frac{q_{air,inf}-q_{O_2,inf}}{M_{N_2}} \tag{45}$$

The mass flow rate of vapor at the stack's outlet could be derived in the same way as the vapor at the inlet as Eq. (46). The total outlet mass flow rate and the vapor part from reaction generation is then obtained as Eqs. (47–48). The vapor source term is finally obtained as Eq. (49).

$$q_{vap,outf}=\frac{n_{air,outf}\cdot RH_{outf}\cdot P_{sat}\left(T_{outf}\right)}{P_{outf}-RH_{outf}\cdot P_{sat}\left(T_{outf}\right)}\cdot M_{vap} \tag{46}$$

$$q_{c,outf}=q_{air,outf}+q_{vap,outf} \tag{47}$$

$$q_{vap,gen}=q_{vap,\ outf}-q_{vap,inf} \tag{48}$$

$$S_{vap}=\frac{10^6q_{vap,gen}}{N\cdot V_c} \tag{49}$$

The generated vapor in each cell which is mentioned in the FNM model is expressed as Eq. (50).

$$q_{c,vap}=\frac{q_{vap,gen}}{N} \tag{50}$$

The momentum source term in the porous medium is expressed by Eq. (51),

$$\mathbf{S}_u=-\frac{\mu_g}{K_g}\vec{u}_g-C_2\frac{1}{2}\rho\left|\vec{u}_g\right|\vec{u}_g \tag{51}$$

The boundary conditions include: the mass flow rate inlet (Eq. (4)), the mass fraction of oxygen and vapor at the inlet and outlet (Eqs. (52–55)), the pressure outlet which is set as the experimental outlet static pressure. The rest surfaces in the stack are all treated as wall.

$$Y_{O_2,inf}=\frac{q_{O_2,inf}}{q_{c,inf}} \tag{52}$$

$$Y_{vap,inf}=\frac{q_{vap,inf}}{q_{inf}} \tag{53}$$

$$Y_{O_2,outf}=\frac{q_{O_2,outf}}{q_{c,outf}} \tag{54}$$

$$Y_{vap,outf}=\frac{q_{vap,outf}}{q_{c,outf}} \tag{55}$$

3. Numerical methods of CFD simulation and experimental test

As indicated above the entire computational domain for the INFM is composed of two regions, the manifold and the header part which is discretized by grids, and the porous medium part for which the experimentally-determined porosity is 0.6543. In order to compare the results obtained by INFM, CFD simulation for retire domain is also conducted.

3.1. Mesh generation and grid-independence test

The bipolar plate features a complex gas channel design, including allocation and collection areas as illustrated in Fig. 4(a). It is to be noted that due to confidentiality considerations, Fig. 4 presents a representative similar schematic rather than the exact structure used in this study, while still sufficiently demonstrating the research methodology. In 3D CFD modeling, constructing the flow field grid strictly according to the gas channel's geometry would result in an estimated 5 billion cells for the 140-cell stack's cathode. To reduce the total grid number, the cathode grid was divided into two distinct regions. The first region (comprising the header, inlet/outlet manifold) maintains a geometry-conforming mesh. The second region simplifies the connecting bridge and the cathode gas channels as a porous medium as Fig. 4 (b). Grid independence tests were conducted separately for both regions to validate the pressure drop calculations. For the simplicity of presentation, the details of the grid-independence are not shown in this paper and can be found in previous work [15]. After the grid-independent test, the final mesh count for the cathode of the 15-cell stack totals 11.64 million. For the 140-cell stack' cathode, the total grid number sums up to 96.14 million. To the authors' knowledge such fine grid-network for the study

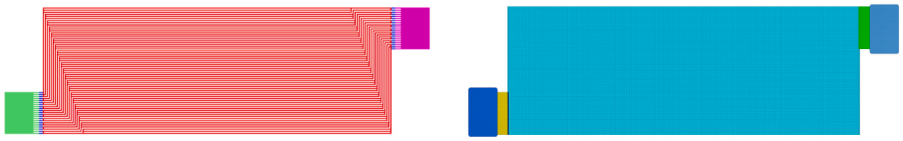

(a) Real configuration (b) Porous medium simplification

Fig. 4. The gas channel of the bipolar plate.

of PEMFC-stack maldistribution is seldom adopted in literature.

3.2. Numerical methods

The governing equations and convection terms are discretized according to the method presented in Ref. [16]. The Reynolds number at the cathode inlet reaches 1.66×10^5. Consequently, the standard k-ε turbulence model is adopted and matched with 'Enhanced wall treatment' to deal with boundary layer. The bridge and reaction zones of cells are set as laminar zones in the Cell Zone Conditions where Reynolds number is well below 2300. Pressure-velocity coupling is resolved via the SIMPLE algorithm, with source terms linearized for numerical treatment. Simulations are performed using Fluent 19.0 with in-house User-Defined Functions (UDF). Additionally, an in-house Improved flow network method (IFNM) was developed in C within the Visual Studio 2022 environment.

3.3. Experimental tests of the two stacks

Experiments on both 15-cell and 140-cell stacks were performed using a custom-developed test platform in the East Electric Hydrogen Fuel Cell Technology *Co*. During testing, system performance was monitored and adjusted by several key parameters: mass flow rate, static pressure, relative humidity, and temperature at stack's inlet and outlet. For the details and the picture of the test facility, Ref [13] can be consulted.

4. Results and discussion

4.1. IFNM porous medium parameters determination based on test of 15-cell stack and reliability verification

Firstly, for determining the parameters related to the porous medium assumption, a group of experiments are carried on the 15-cell stack. The operating conditions on the stack's cathode at 0.3, 0.6, 0.8, 1.0, 1.4, 1.8 A/cm^2 are listed in Table 1.

The mass flow rate to experimental pressure drop relationship is shown in Fig. 5 as the dash line. As seen in the figure good agreement is obtained.

It may be noted that the local validation (per-branch or per-group flow measurements, pressure taps along manifolds) for a PEMFC stack is practical impossible because of the difficulty in obtaining such data [20]. The experimental data in this study were obtained through collaboration with Chengdu Dongqi Hydrogen Energy *Co*., Ltd., using a commercially available industrial stack that is prohibitively expensive to modify. Fortunately, the main subject of this article is comparing CFD simulation with IFNM simulation for predicting the maldistribution of a complex flow field structure. In this comparison, we take the results of CFD as the comparison reference.

The determination process of the porous medium parameters, including the viscous resistance $\frac{1}{K_g}$ and the inertial resistance C_2, have been introduced in Ref [13]. For the IFNM, the best-fit porous medium parameters are determined as $\frac{1}{K_g} = 3.48 \times 10^8\ m^{-2}, C_2 = 450\ m^{-1}$. The results from IFNM by using these two values are shown in Fig. 5 with black-solid line. Meanwhile, because the CFD analysis includes the gas flow in three directions, the best-fit porous medium parameters for the CFD analysis are different from those of the IFNM and are determined as: $\frac{1}{K_g} = 2.30 \times 10^8\ m^{-2}, C_2 = 250\ m^{-1}$. The CFD pressure drop using these two values are shown in Fig. 5 with blue solid line. The relative deviations in pressure drop between the simulation and experiment are all well below 10 % for both CFD and IFNM, with the exception of the first point which reaches around 15 % likely due to the measurement uncertainty. The relative deviations of the pressure drop between CFD and IFNM results are within 4 % at the six operating conditions.

To further verify the reliability of the two numerical values of the porous medium parameter, they are subsequently used in simulation for six extra experimental operating conditions as robustness verification (listed in Table 2).

Compared with the experimental data, the relative difference of pressure drop of these 6 cases for both simulation methods are all found within 10 % as shown in Table 3.

The agreement between simulation and experimental results demonstrates that the porous medium flow region with the determined parameters can accurately represent the real cathode gas channel. In the

Table 1
The working conditions in the 15-cell stack's cathode experiment.

j /A. cm^{-2}	$q_{c,inf}$ / kg. s^{-1}	P_{in} / Pa	P_{out} / Pa	T_{in} / K	T_{in} / K	RH_{in}	RH_{out}
0.3	2.12×10^{-3}	10,747	5226	316.1	318.7	0.91	1.00
0.6	2.37×10^{-3}	29,963	25,026	326.1	331.0	0.57	1.00
0.8	3.28×10^{-3}	22,057	14,447	340.4	336.0	0.66	0.88
1.0	3.85×10^{-3}	55,068	42,900	336.3	331.2	0.30	1.00
1.4	5.61×10^{-3}	59,832	48,637	343.3	350.0	0.50	0.71
1.8	6.73×10^{-3}	73,332	59,376	350.7	359.4	0.59	0.64

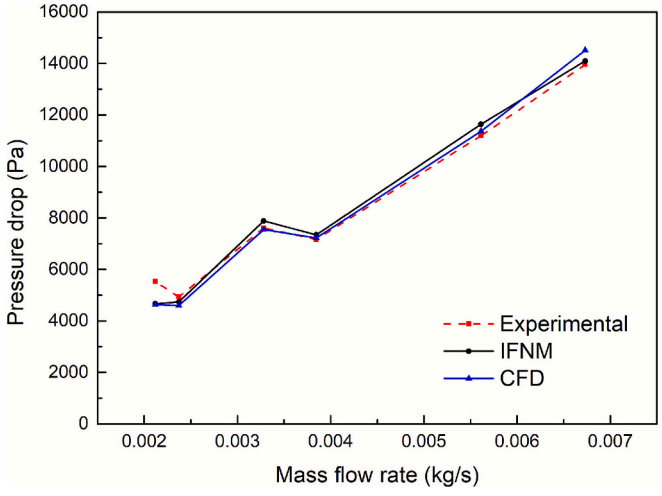

Fig. 5. 15-cell stack experimental pressure drop and analysis pressure drop.

Table 2
The additional working conditions at 1.0 A/cm^2, 1.8 A/cm^2.

No.	j /A.cm^{-2}	$q_{c,inf}$ / kg.s^{-1}	P_{in} / Pa	P_{out} / Pa	T_{in} / K	T_{in} / K	RH_{in}	RH_{out}
1	1.0	3.567×10^{-3}	49,905	42,637	331.2	336.6	0.50	1.00
2	1.0	3.652×10^{-3}	49,858	41,595	332.1	337.7	0.75	1.00
3	1.0	3.714×10^{-3}	49,863	41,289	333.7	339.5	0.87	1.00
4	1.8	5.890×10^{-3}	66,411	53,611	350.3	358.8	0.35	0.54
5	1.8	6.757×10^{-3}	83,128	68,260	351.9	360.2	0.54	0.60
6	1.8	6.720×10^{-3}	100,020	86,768	350.9	359.1	0.58	0.67

Table 3
The pressure drop relative deviation at different operating conditions.

No.	j /A. cm^{-2}	ΔP_{exe} / Pa	ΔP_{IFNM} / Pa	Relative deviation	ΔP_{CFD} / Pa	Relative deviation
1	1.0	7268	7481	2.93 %	7342	1.01 %
2	1.0	8263	7748	−6.23 %	7636	−7.59 %
3	1.0	8574	8009	−6.59 %	7856	−8.38 %
4	1.8	12,800	13,721	7.20 %	13,378	4.51 %
5	1.8	14,868	15,018	1.01 %	14,720	−0.99 %
6	1.8	13,252	13,452	1.51 %	13,238	−0.11 %

following the maldistribution studies are mainly conducted by the IFNM, however, for comparison purpose, CFD simulations are also conducted for some cases.

4.2. The cathode gas distribution in the 140-cell stack and IFNM distribution verification

The verification in the previous part has confirmed that the porous-medium-simplified channels demonstrate flow-pressure behavior equivalent to actual cathode channels. Since the flow resistance of each single cell depends solely on its channel geometry (remaining constant regardless of stack's cell number) and both 15-cell and 140-cell stacks use identical cells, we validly apply the established porous medium parameters to simulate the 140-cell stack, following the methodology in works [15,16]. The experiment operating conditions of the three experiments are listed in Table 4 at 0.3, 1.0, 1.8 A/cm^2 on the 140-cell stack. Simulations are taken by both the IFNM and CFD method for comparison.

The mass flow rate at the inlet bridge of each unit cell is monitored to evaluate gas maldistribution using two indices established in [16]: the relative deviation of mass flow rate $\overline{q_j}$, defined by Eq. (56), which characterizes the air distribution curve (ADC). Rather than the mean squared error of mass flow rate, the distribution range $R_{\overline{q_j}}$, given by Eq. (57), is chosen to evaluate the distribution uniformity, where a smaller value indicates better flow uniformity. This is due to the bucket effect, cells with the lowest reactant concentration become the performance bottleneck of the entire fuel cell stack.

$$\overline{q_j} = \frac{q_{bin,j} - q_{bin,ave}}{q_{bin,ave}} \tag{56}$$

$$R_{\overline{q_j}} = \frac{q_{bin,max} - q_{bin,min}}{q_{bin,ave}} \tag{57}$$

Table 4
The working condition of 140-cell stack's cathode.

j /A. cm^{-2}	ΔP_{exe} / Pa	ΔP / kPa	P_{out} / kPa	T_{in} / K	T_{out} / K	RH_{in}	RH_{out}
0.3	1.81×10^{-2}	3.5	3.0	316.15	318.15	0.92	1.00
1.0	3.48×10^{-2}	8.0	12.0	336.15	340.15	0.65	0.88
1.8	6.31×10^{-2}	12.0	64.0	339.15	346.15	0.43	0.80

For the 140-cell stack under three operating conditions with cell number after Fig. 1, the absolute mass flow rate variations obtained from both methods are presented in Figs. 6(a)–6(c). Fig. 6(d) illustrates the variation of the relative mass flow rate deviation $\overline{q_j}$, referred to as the air distribution curve. The results demonstrate strong agreement between the IFNM and CFD models, both in terms of the overall distribution trend of cathode gas and the absolute mass flow rate values across individual cells.

As far as the value of $R_{\overline{q_j}}$ is concerned, the CFD $R_{\overline{q_j}}$ at 1.8, 1.0, 0.3 A/cm^2 is 7.35 %, 5.10 %, and 3.27 %, respectively. While for the IFNM, $R_{\overline{q_j}}$is 7.69 %, 5.16 % and 3.23 %, respectively. Since the two methods are based on consistent assumptions and IFNM takes much less times to reach the accuracy of CFD analysis in this study, which once again proves the reliability of the IFNM distribution analysis.

Both results of the two methods show that there are two features of the gas maldistribution variation with current and cell number. First, the maldistribution of the gas flow rate becomes more severe with the current density increase. Second, there is a turning point of cell number, around at the location of the 60th cell, for the 140-cell stack's cathode flow maldistribution. For this call its flow rate equals the averaged value. Beyond this cell number, the maldistribution is alleviated with the decrease in cell number, while less than this cell number, gas flow maldistribution decreases with the increase of cell number. Meanwhile, $R_{\overline{q_j}}$values are all under 10 %, which proves that this 140-cell stack enjoys a quite good uniform distribution even at high current density operating condition.

The velocity distribution from CFD result at 1.0 A/cm^2 is shown in Fig. 7 which demonstrates the velocity vectors in the A-A' and B-B′ sections. As seen from Figs. 7 (b) and (c), the velocity basically changes little from the header to the inlet manifold, which means the header does not bring in strong inlet effect such as strong acceleration or recirculation to the gas entering in the manifold. It is for this reason that the ADCs obtained through CFD demonstrate comparability with those derived from IFNM, since both methodologies are predicated on the absence of external influences. Concurrently, the flow distribution as indicated by the ADC profile is relative satisfying because the header does not induce unduly strong vortices that would lead to flow starvation in the stack's upstream cells.

4.3. The necessity of explicit vapor generation modeling in stack's cathode analysis

In the conventional studies of the stack maldistribution ([3,6–8,18]), the vapor generated during the reaction is usually ignored. In this study, this factor is taken into account based on available test data explicitly. According to experimental data, the mass fraction of generated vapor at the outlet $Y_{vap,gen,out}$ and the ratio of generated vapor to the consumed oxygen mass flow rate $q_{vap,gen} : q_{o_2,con}$ at the three operating conditions of the 140-cell stack are calculated and shown in Table 5.

From Table 5, there's an obvious increase of the relative humidity from the stack's inlet to the outlet. It also shows that the vapor generated in reaction takes up a higher percentage of the gas at the outlet with increasing current density. At the 1.8 A/cm^2, the quantity of vapor generation equals 67 % of that of oxygen consumption. In the other word, the generated vapor gradually becomes considerable to the total

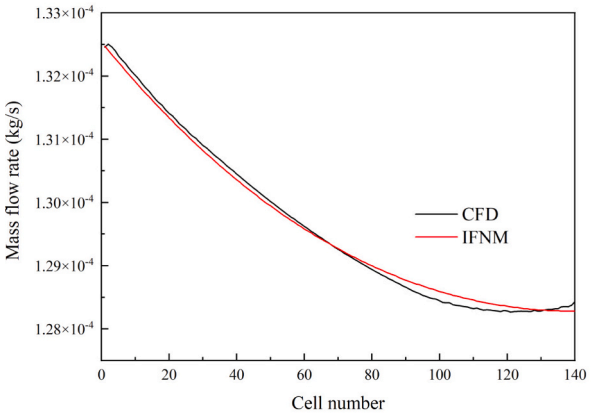

(a) variation of absolute mass flow rate at 0.3 A/cm

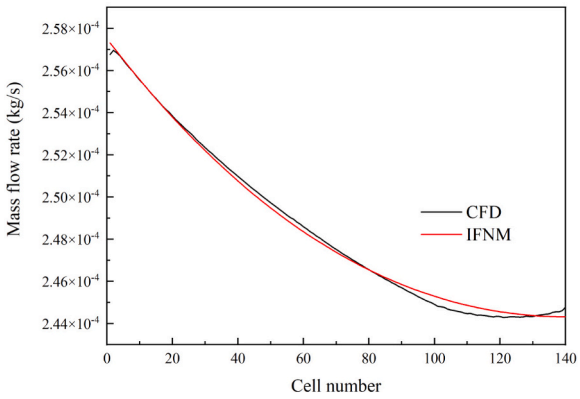

(b) variation of absolute mass flow rate at 1.0 A/cm^2

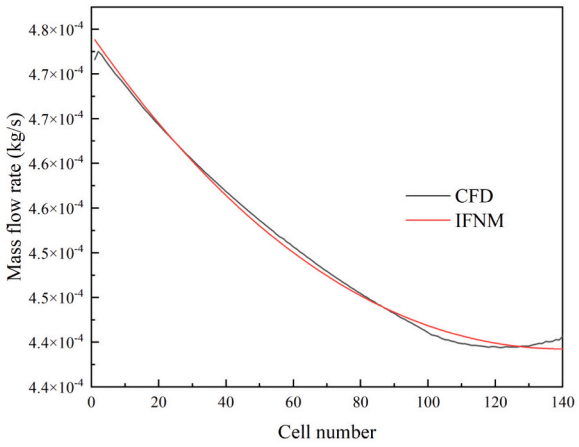

(c) variation of absolute mass flow rate at 1.8 A/cm^2

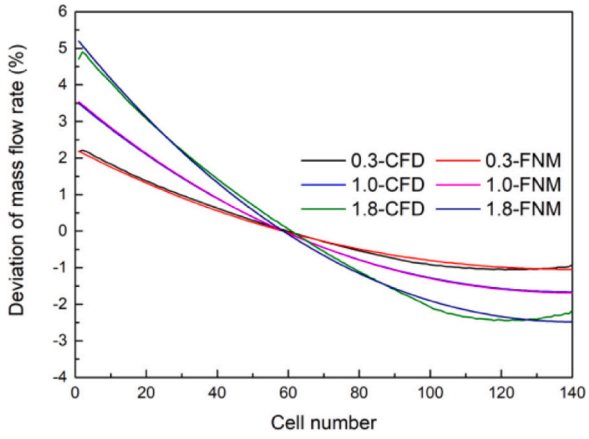

(d) relative mass flow rate deviation (ADCs)

Fig. 6. Variation trend of 140-cell stack cathode between IFNM and CFD.

mass change in the stack as current density increases. On the condition that the large-scale PEMFC stack normally works at higher current density, the vapor generation should also be consequently added into the investigation model since the oxygen consumption has been included in most present studies of the stack gas maldistribution.

To further investigate the influence of vapor generation, Fig. 8 compares the ADCs based on the IFNM with and without accounting for vapor generation. As shown in Figs. 8, at 0.3 A/cm^2, the distribution range of with and without is 3.23 % and 3.18 %, respectively. ADCs of the two assumptions shows negligible differences with or without considering vapor generation, suggesting vapor generation can be ignored for low current density. However, the difference becomes progressively more significant with increasing current density. At 1.0, 1.8 A/cm^2, the distribution range with consideration of vapor generation equals respectively 5.16 % and 7.69 %, respectively. While without this consideration, it equals 4.70 % and 6.90 %, respectively. This demonstrates ignoring vapor generation will underestimate the maldistribution. Consequently, the vapor generation should be taken into account for the accurate maldistribution analysis especially for high current density working conditions for large stack. These findings prove explicit vapor generation modeling as fundamental and innovative to the IFNM methodology, equally critical as the porous medium simplification for flow field.

4.4. Complete study of the effects of geometric factors for gas distribution uniformity in the stack's cathode

The CFD simulation of the 140-cell stack conducted in this paper usually needs nearly 48 h with 508 processes working together to reach full convergence for one case. While based on the condition that the inlet effect is ignorable, the IFNM just takes a few seconds with Intel i7-6500U 4 cores to get the distribution results very close to the CFD result.

Consequently, the INFM is adopted to analyze a group of geometric sizes selected to discuss their influence on the cathode gas maldistribution. The selected six geometric parameters include the width, the length of both manifold cross-sections w_{mf}, L_{mf}, the width, the height and the length of both bridge w_b, h_b, L_b and the height of each manifold segment h_s as illustrated in Fig. 9. The six parameters are selected for their close correlation with the manifold structure. In particular, the influence of bridge geometry on distribution uniformity—specifically its effect trend and relative importance compared to manifold cross-sectional parameters—has not been adequately studied and thus requires systematic investigation. In contrast, well-established parameters such as the number of cells (i.e., total manifold height), which have been consistently reported in the literature, are excluded to avoid redundant analysis.

For the convenience of discussion, the factors are normalized based on their original sizes shown in Table 6. Each factor varies on four levels

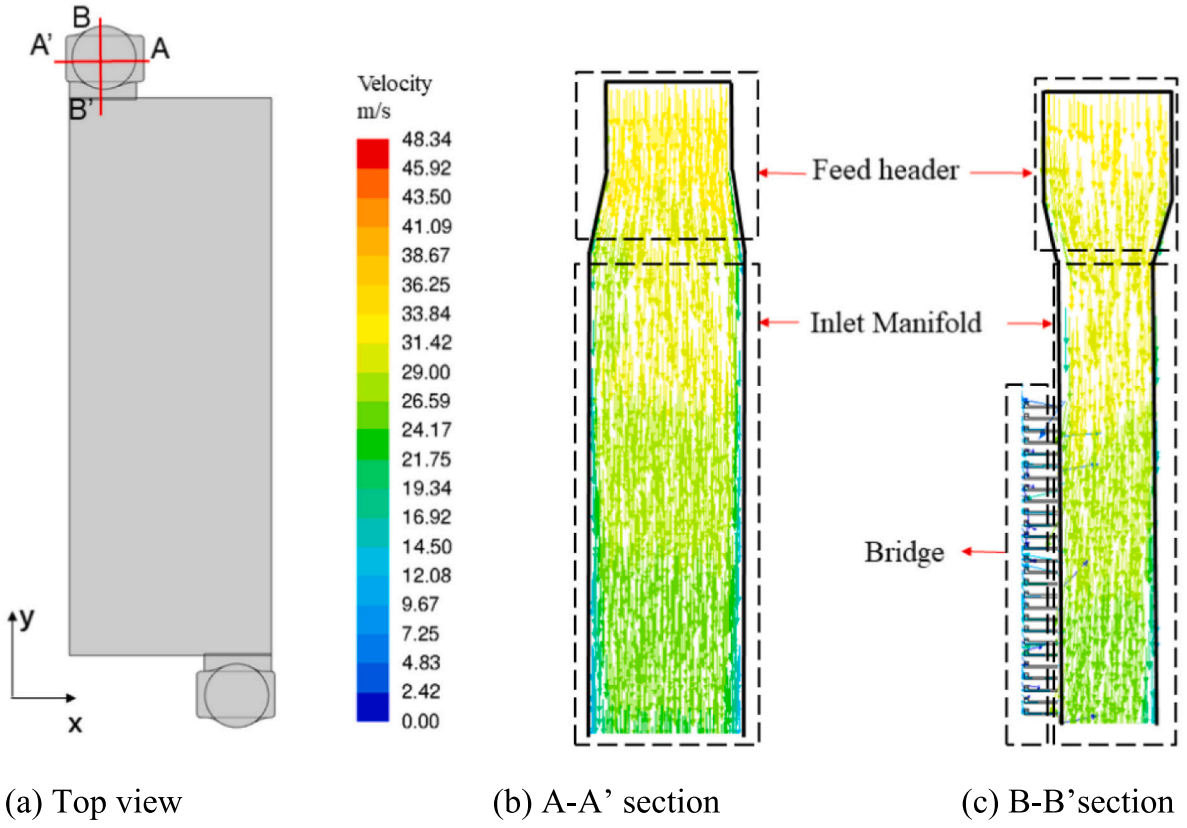

Fig. 7. The velocity vector in the inlet manifold at 1.0 A/cm^2.

Table 5
The related data of vapor in the 140-cell cathode.

j_c / A.cm^{-2}	$Y_{vap,in}$	$Y_{vap,out}$	$Y_{vap,gen,out}$	$q_{vap,gen}$: $q_{o_2,con}$
0.3	4.73 %	5.99 %	1.00 %	0.16
1.0	7.97 %	14.54 %	6.17 %	0.55
1.8	7.31 %	21.57 %	13.77 %	0.67

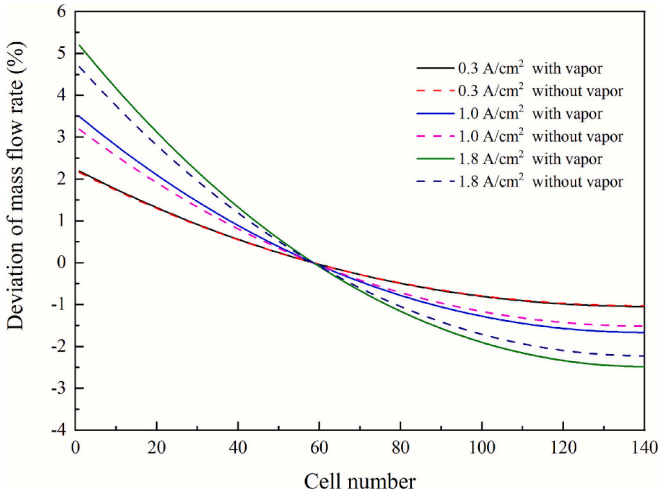

Fig. 8. The difference of maldistribution tendency with and without considering vapor generation.

numbered as 1 to 4. In the study the variation of each factor is independent on each other.

Since the IFNM calculation time for a single case only takes seconds, it is applicable to carry out a full factor numerical design for the effects of six geometric factors instead of the orthogonal experiment design. The total times of numerical experiments is $4^6 = 4096$ and it takes around 16 min to complete the computation. The adopted operating condition is at 1.8 A/cm^2.

To evaluate their influences, the Range analysis is adopted and the results are recorded in Table 7. In this table, each of six factors got their own T_i, which represents the sum of the numerical target value $R_{\overline{q_j}}$ of the cases at level i ($i = 1,2,3,4$) for this factor as shown in Eq. (60). Because the target value $R_{\overline{q_j}}$ represents the maldistribution degree and T_i is the sum of $R_{\overline{q_j}}$ for certain cases, the lower T_i, the less maldistribution shall this factor bring to the stack when it's at level i.

$$T_i = \sum R_{\overline{q_j}} \tag{60}$$

Meanwhile, t_i represents the ratio of T_i to the total experiment times at this level i as defined by Eq. (61).

$$t_i = \frac{T_i}{N} \tag{61}$$

A parameter R_T is introduced to represents the max-min value of T_i for one of the factors as defined in Eq. (63). Its value indicates the variation range of the experimental target value when the levels of each column factor change. The larger the value, the greater impact shall this factor brings to the stack's maldistribution. By ranking R_T of the six factors according to their value, it is able to determine their impacting strength, which reflects the importance of the influence to the maldistribution.

$$R_T = T_{i,\max} - T_{i,\min} \tag{63}$$

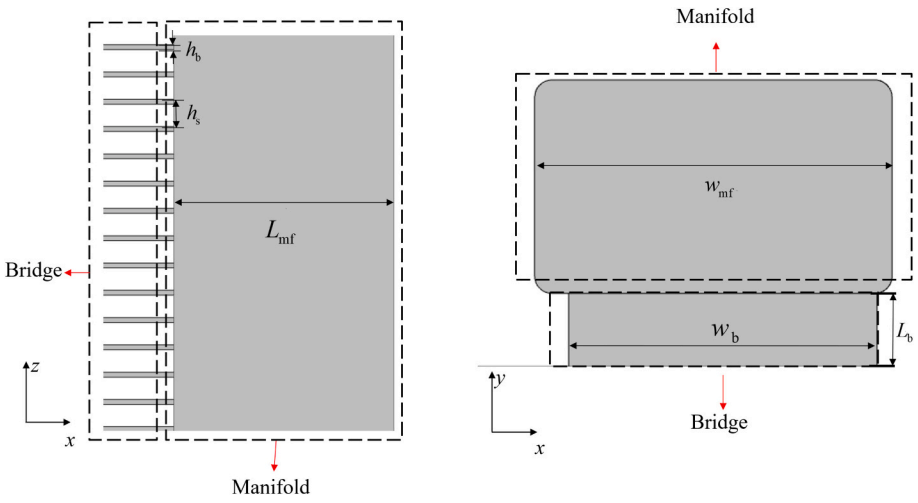

Fig. 9. The six geometric factors for the full factor numerical experiment.

Table 6
Six factors and four levels design.

Level	Factors					
	A	B	C	D	E	F
	$w_{mf} : w_{mf_0}$	$L_{mf} : L_{mf_0}$	$w_b : w_{b_0}$	$h_b : h_{b_0}$	$L_b : L_{b_0}$	$h_s : h_{s_0}$
1	0.9	0.9	0.8	0.9	0.9	0.9
2	1.0	1.0	0.9	1.0	1.0	1.0
3	1.1	1.1	1.0	1.1	1.1	1.1
4	1.2	1.2	1.034	1.2	1.2	1.2

Table 7
Numerical results.

Factor	A	B	C	D	E	F
T_1	89.676	90.158	63.960	63.974	70.356	66.695
T_2	72.462	72.513	67.280	66.993	68.737	67.566
T_3	59.755	59.559	69.989	69.482	67.192	68.437
T_4	50.112	49.774	70.775	71.555	65.719	69.307
t_1	0.08757	0.08804	0.06246	0.06248	0.06871	0.06513
t_2	0.07076	0.07081	0.06570	0.06542	0.06713	0.06598
t_3	0.05835	0.05816	0.06835	0.06785	0.06562	0.06683
t_4	0.04894	0.04861	0.06912	0.06988	0.06418	0.06768
Best	4	4	1	1	4	1
R_T	39.564	40.383	6.814	7.581	4.637	2.612
Rank	B > A> > D > C > E > F					

To visually demonstrate the relationship between the factors and the cathode maldistribution, Figs. 10(a ~ f) are drawn with the factor's level as x-axis and t_i as y-axis. Fig. 10 indicates that t_i shall decrease with the increase of factors of A, B and E (effects of w_{mf}, L_{mf} and L_b) and increase with the increase of factors of C, D and F (effects of w_b, $h_b$and h_s).

According to Table 7,the impacting strength is determined as: $L_{mf} : L_{mf_0}$(B) $> w_{mf} : w_{mf_0}$(A) $> h_b : h_{b_0}$(D)> $w_b : w_{b_0}$(C) $> L_b : L_{b_0}$(E)>$h_s : h_{s_0}$(F). Besides, as shown in Fig. 9, the relationships of the 6 factors with the maldistrubution degree are all monotonic.

Physically it is easy to understand that the influences of A and B (effects of the geometric size of w_{mf} and L_{mf}) surpass other parameters. The increase of their size contributes to a reduction in axial velocity in the inlet manifold which is the crucial part for distribution. Consequently, the dynamic pressure of the inlet fluid decreases. According to Bernoulli's principle, this results in an increase in static pressure and, more importantly, a more gradual static pressure gradient along the length of the manifold, which will evidently improve the cathode distribution uniformity. While B and A have comparable impact factors, this conclusion is based on the premise of scaling them proportionally. Therefore, if the goal is to increase both by the same absolute length, expanding L_{mf} would be the more economical choice for distribution uniformity improvement. According to the results of the full-factor analysis, compared with the original case when L_{mf} is lengthened to 1.1 times and 1.2 times, the maldistribution factor $R_{\overline{q_j}}$ turns out to be 6.32 % and 5.28 %, which decreases by 17.8 % and 31.3 % respectively. Since their influences are the strongest, ANCOVA is adopted to analyze A and B's interaction. The result shows that the coefficient of A*B is 242, which means both their increase will help to expand the improvement by another factor's increase.

The influence of the factors C, D and E (effects of w_b, h_b, L_b), are relatively limited compared with A and B. This is due to the fact that the pressure change in the fuel cell's bridge merely takes up a limited percentage in the whole change. Within them, D (effect of height h_b) has relative higher impact strength while E (effect of bridge length L_b) has relative lower impact strength. However, L_b displays opposite influence to the other two factors that lengthening L_b will improve distribution uniformity. For the other two factors, decreasing h_b and w_b will help to improve cathode gas maldistribution.

For the last factor D (effect of h_s), its impacting strength is the weakest among the six factors. Consequently, controlling the length of h_s won't be main concern to the improvement measures if there's not much limit to the PEMFC stack's height.

Based on the above results the factors C, D, E, F have less influence on the stack maldistribution. To improve the stack maldistribution effectively, it is recommended to lengthen the w_{mf} and L_{mf}. For this study, it is suggested to both increase L_{mf} and w_{mf} to 1.2 times, and the maldistribution indicator $R_{\overline{q_j}}$ will decease to 3.64 %.

5. Conclusion

1) An improved flow network method (IFNM) is proposed, characterized by the adoption of a porous-medium pressure-drop formulation for flow-field representation and the explicit consideration of vapor generation in the cathode. In addition, the porous-medium parameters are accurately identified from the measured relationship between flow rate and pressure drop under real operating conditions, and their stability is further verified through robustness tests. IFNM can be generalized and applied to complex flow fields analogous to the one examined in this work.

2) For the complex flow field structure studied in this paper, deviations in distribution range value by CFD and IFNM are below 5 %. The prediction of the cathode flow maldistribution by IFNM only takes several seconds while by CFD several ten hours are needed. The proposed IFNM offers a fast and accurate method for improving the gas

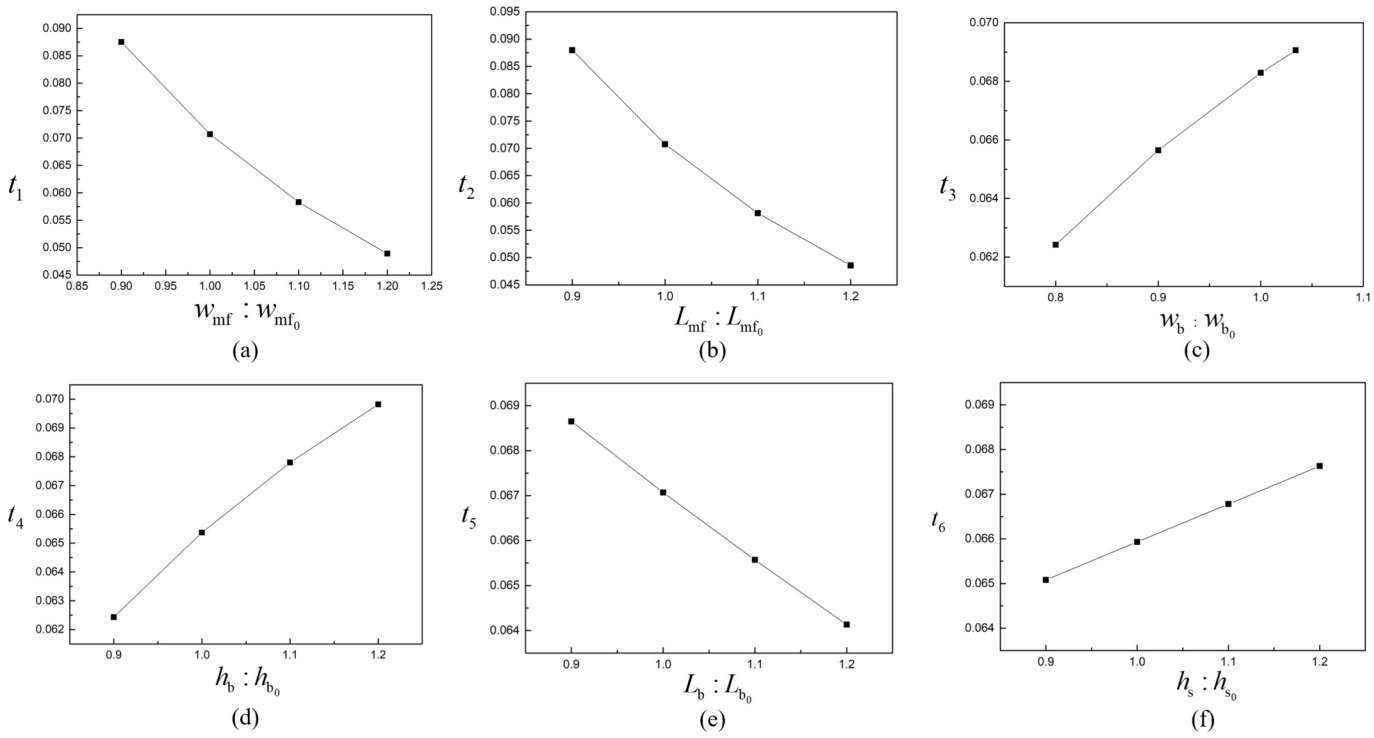

Fig. 10. The relationships between factors and target values.

maldistribution of PEMFC stack at the condition of ignorable inlet effect.

3) The quantity of the vapor generation is an important influencing factor when analyzing the cathode gas distribution uniformity. The gas distribution tendency obtained from FNM shows an evident error if the vapor generation is not considered at high current density operating condition. The explicit vapor generation modeling is necessary for cathode distribution analysis.

4) A full factor numerical design for the six geometric sizes of the manifold is conducted by the IFNM to study their influence to the 140-cell stack's cathode maldistribution. Results show that the most influencing factors are the manifold length L_{mf} and width w_{mf}. For example, by increasing L_{mf} to 1.2 times, the maldistribution indicator $R_{\overline{q_j}}$ will be reduced to 5.28 % compared with 7.69 % of the original case. By increasing L_{mf} and w_{mf} to 1.2 times, $R_{\overline{q_j}}$will decease to 3.64 %.

CRediT authorship contribution statement

Ren-Jie Yin: Writing – review & editing, Writing – original draft, Validation, Software, Resources, Methodology, Investigation, Formal analysis, Data curation, Conceptualization. **Fan Bai:** Resources, Methodology. **Yu-tong Mu:** Methodology. **Li Chen:** Supervision, Resources. **Wen-Quan Tao:** Writing – review & editing, Supervision.

Declaration of competing interest

The authors declare that they have no known competing financial interests or personal relationships that could have appeared to influence the work reported in this paper.

Acknowledgment

Supports from the S&T Program of Energy Shaanxi Laboratory (ESLB202408), from the National Natural Science Foundation of China for Young Researchers (52306112), the Project of Shaanxi Innovative Talent Promotion Plan-Technology Innovation Team (No. 2024RS-CXTD-35) are greatly acknowledged.

Data availability

Data will be made available on request.

References

[1] E.D. B. Baca, C. Fujimoto, H. Chung, Y.S. Kim, Highly quaternized polystyrene ionomers for high performance anion exchange membrane water electrolysers, Nat. Energy 5 (5) (2020) 378–385.
[2] F. Bai, L. Lei, Z. Zhang, L. Chen, L. Chen, W.Q. Tao, Application of similarity theory in the study of proton exchange membrane fuel cells: a comprehensive review of recent developments and future research requirements, Energy Storag. Saving 1 (1) (2022) 3–21.
[3] J. Park, X. Li, Effect of flow and temperature distribution on the performance of a PEM fuel cell stack, J. Power Sources 162 (1) (2006) 444–459, https://doi.org/10.1016/j.jpowsour.2006.07.030.
[4] H. Chen, S.P. Jung, S.C. Yen, Flow distribution in the manifold of PEM fuel cell stack, J. Power Sources 173 (1) (2007) 249–263, https://doi.org/10.1016/j.jpowsour.2007.05.007.
[5] J. Wang, H. Wang, Discrete method for design of flow distribution in manifolds, Appl. Therm. Eng. 89 (2015) 927–945, https://doi.org/10.1016/j.applthermaleng.2015.06.069.
[6] A. Amirfazli, S. Asghari, M. Sarraf, An investigation into the effect of manifold geometry on uniformity of temperature distribution in a PEMFC stack, Energy 145 (2018) 141–151, https://doi.org/10.1016/j.energy.2017.12.124.
[7] Y. Qin, G. Liu, Y. Chang, Q. Du, Modeling and design of PEM fuel cell stack based on a flow network method, Appl. Therm. Eng. 144, no. January (2018) 411–423, https://doi.org/10.1016/j.applthermaleng.2018.08.050.
[8] F. Huang, D. Qiu, S. Lan, P. Yi, L. Peng, Performance evaluation of commercial-size proton exchange membrane fuel cell stacks considering air flow distribution in the manifold, Energy Convers. Manag. 203 (October 2019) (2020) 112256, https://doi.org/10.1016/j.enconman.2019.112256.
[9] F. Huang, D. Qiu, Z. Xu, L. Peng, X. Lai, Analysis and improvement of flow distribution in manifold for proton exchange membrane fuel cell stacks, Energy 226 (2021) 120427, https://doi.org/10.1016/j.energy.2021.120427.
[10] G. Su, D. Yang, Q. Xiao, H. Dai, C. Zhang, Effects of vortexes in feed header on air flow distribution of PEMFC stack: CFD simulation and optimization for better uniformity, Renew. Energy 173 (2021) 498–506.
[11] W.H. Chen, Z.L. Tsai, M.H. Chang, S. You, P.C. Kuo, Geometry optimization and pressure analysis of a proton exchange membrane fuel cell stack, Int. J. Hydrog. Energy 46 (31) (2021) 16717–16733.
[12] W. Pan, Z. Chen, X. Chen, F. Wang, G. Dai, Analytical and numerical investigation of flow distribution in PEMFC stacks, Chem. Eng. J. 450 (2022) 137598.
[13] S. Hossein, A. Nima, M. Iraj, A. Majid, The study of cylindrical polymer fuel cell's performance and the investigation of gradual geometry changes' effect on its

performance, Periodica Polytechnica, Chem. Eng. (2019) 63, https://doi.org/10.3311/PPch.12793.
[14] F. Huang, D. Qiu, L. Peng, X. Lai, Optimization of entrance geometry and analysis of fluid distribution in manifold for high-power proton exchange membrane fuel cell stacks, Int. J. Hydrog. Energy 47 (52) (2022) 22180–22191.
[15] F. Bai, R. Yin, J. Liao, Z. Zhang, S. Cai, Y. Mu, W. Tao, Eccentricity design for the coolant distribution optimization of a practical commercial-size proton exchange membrane fuel cell stack using a novel proper orthogonal decomposition based analysis model, Appl. Energy 347 (2023) 121389.
[16] R. Yin, W. Zeng, W. C., F. Bai, L. Chen, W. Tao, Study on the effects of manifold structure on the gas flow distribution uniformity of anode of PEMFC stack with 140-cell, Renew. Energy 221 (2024) 119693.
[17] T. Huang, W, W. Ding, Y. Xiao, R. Ke, P. Zou, Y. Chen, Z. Wan, Z. Tu, W. Zeng, Manifold geometry optimization and flow distribution analysis in commercial-scale proton exchange memberane fuel cell stacks, Renew. Energy 237 (2024) 121736.
[18] L. Xian, Q. Wang, Z. Li, S. Li, S. Lv, Y. Yu, L. Chen, W. Tao, Analyzing and optimizing cathode gas distribution uniformity in proton exchange membrane fuel cell stacks based on two-phase flow network model, J. Power Sources Volume 618 (2024) 235182. ISSN 0378–7753, https://doi.org/10.1016/j.jpowsour.2024.235182.
[19] X. Yu, X. Chen, R. Huang, J. Chen, M. Bao, H. He, L. Wang, G. Lu, Optimization of manifold structural parameters for high-power proton exchange membrane fuel cell stack, Int. J. Hydrog. Energy 100 (2025) 921–935. ISSN 0360-3199, https://doi.org/10.1016/j.ijhydene.2024.12.096.
[20] Nima Ahmadi, Ghader Rezazadeh, Polymer electrolyte membrane fuel cell performance Revolutionized: Artificial intelligence-validated asymmetric flow channels enhance mass transport via hybrid analytical-numerical frameworks, Case Stud. Therm. Eng. 73 (2025) 106445. ISSN 2214-157X, https://doi.org/10.1016/j.csite.2025.106445.
[21] Ahmad Rezaei, Mazaher Rahimi-Esbo, Kamran Dadashi Firouzjaei, Ebrahim Alizadeh, Experimental and numerical investigation on the oxygen distribution in the cathode section of a PEMFC stack, Renewable Energy, Volume 256, Part B (2026) 123996. ISSN 0960-1481, https://doi.org/10.1016/j.renene.2025.123996.
[22] M. Sahraoui, Y. Bichioui, K. Halouani, Three-dimensional modeling of water transport in PEMFC, Int. J. Hydrog. Energy 20138 (2013) 8524–8531.
[23] T. Cao, Y. Mu, J. Ding, H. Lin, Y. He, W. Tao, Modeling the temperature distribution and performance of a PEM fuel cell with thermal contact resistance, 2015, Int. J. Heat Mass Transf. 2015 (87) (2015) 544–556.
[24] Y. Mu, P. He, J. Ding, W. Tao, Modeling of the operation conditions on the gas purging performance of polymer electrolyte membrane fuel cells, Int. J. Hydrog. Energy 2017 (42) (2017) 11788–11802.
[25] G. Zhang, K. Jiao, Multi-phase models for water and thermal management of proton exchange membrane fuel cell: a review, J. Power Sources 2018 (391) (2018) 120–133.
[26] H. Chen, H. Guo, F. Ye, et al., Modification of the two-fluid model and experimental study of proton exchange membrane fuel cells with baffled flow channels, Energy Convers. Manag. 20109 (195) (2019) 972–988.
[27] X. Yan, C. Guan, Y. Zhang, et al., Flow field design with 3D geometry for proton exchange membrane fuel cells, Appl. Therm. Eng. Des. Process. Equip. Econ. 147 (2019) 1107–1114.
[28] Z. Zhang, F. Bai, P. He, Z. Li, W. Tao, A novel cathode flow field for PEMFC and its performance analysis, Int. J. Hydrog. Energy 48 (2023) 24459–24480.
[29] M. Bassett, D. Winterbone, R. Pearson, Calculation of steady flow pressure loss coefficients for pipe junctions, in: Proceedings of the Institution of Mechanical Engineers, Part C: Journal of Mechanical Engineering Science, vol. 215, 2001, p. 861e81. 8.
[30] W. Wu, Z. Wang, A. Revell, P. Jarman, Computational fluid dynamics calibration for network modelling of transformer cooling flows e part II: pressure loss at junction nodes, IET Electr. Power Appl. 6 (1) (2012) 28.
[31] S. Jing, M. Zhang, Mechanics. Fluid Mechanics [M], Xi'an Jiaotong University Press, 2001.
[32] H. Cross, Analysis of Flow in Networks of Conduits or Conductors vol. 286, University of Illinois Bulletin, 1936, p. 42e7. 1.